AGU PUBLICATIONS

JGR

Journal of Geophysical Research: Solid Earth

RESEARCH ARTICLE

10.1002/2013JB010835

On the apparent attenuation in the spatial coherence estimated from seismic arrays

Ravishankar Menon[1], Peter Gerstoft[1], and William S. Hodgkiss[1]

[1]Marine Physical Laboratory, Scripps Institution of Oceanography, University of California, San Diego, La Jolla, California, USA

Key Points:
- Averaging is not always helpful in ambient noise processing and can induce bias
- Higher-mode Rayleigh and P waves contaminate coherences in the microseism band
- Attenuation retrieved from data is mostly due to interference and not intrinsic

Correspondence to:
R. Menon,
rmenon@ucsd.edu

Citation:
Menon, R., P. Gerstoft, and W. S. Hodgkiss (2014), On the apparent attenuation in the spatial coherence estimated from seismic arrays, *J. Geophys. Res. Solid Earth*, *119*, 3115–3132, doi:10.1002/2013JB010835.

Received 8 NOV 2013
Accepted 18 MAR 2014
Accepted article online 20 MAR 2014
Published online 11 APR 2014

Abstract Several recent studies have used the coherence of seismic noise between stations to retrieve the phase slowness and attenuation. However, there is considerable debate on the feasibility of attenuation retrieval, its interpretation, and its dependence on the noise directionality and has been the subject of several analytical and numerical studies. In this article, we perform a detailed analysis of the various factors that play a role in the estimation of spatial coherence and attenuation from seismic arrays using data from the Southern California Seismic Network. For instance, certain common preprocessing steps such as averaging neighboring frequencies to improve the estimate are sufficient to introduce attenuation-like effects. The presence of first-mode surface Rayleigh wave and *P* waves in addition to the fundamental mode in Southern California (at frequencies 0.05–0.2 Hz) suggests that the underlying spatial coherence is better modeled as a linear combination of the above wave types. Although this describes the observed coherence better than a simple zeroth-order Bessel function, the resulting phase cancelations due to the multiple seismic waves can be misconstrued as attenuation if not taken into consideration. Using simulations, we show that due to the slowness inhomogeneity, azimuthally averaging the coherence is not equivalent to homogenizing the medium and instead introduces apparent attenuation in the coherence due to interference. Trying to fit an exponential decay model to this apparent attenuation results in an attenuation coefficient which is similar to previously published results.

1. Introduction

In recent years, there has been widespread interest in using background seismic noise to study and monitor the properties of the Earth at different scales (for a recent review, see *Wapenaar et al.* [2010a, 2010b] and *Snieder and Larose* [2013]). Much of this progress has been possible due to a key observation that the cross correlation of diffuse waves yielded, in expectation, the Green's function of the medium [*Lobkis and Weaver*, 2001; *Weaver and Lobkis*, 2001] and the availability of continuous seismic records going back several decades. Although the underlying theoretical assumptions are seldom satisfied in seismic applications, using noise has been widely successful in robustly retrieving travel times for tomography [*Shapiro et al.*, 2005; *Sabra et al.*, 2005; *Gerstoft et al.*, 2006a; *Yao et al.*, 2006; *Lin et al.*, 2008; *Ekström et al.*, 2009] and understanding its dependency on noise directionality [*Tsai*, 2009; *Yao and Van Der Hilst*, 2009; *Harmon et al.*, 2010], studying surface wave anisotropy [*Fry et al.*, 2010; *Gallego et al.*, 2011; *Riahi and Saenger*, 2014] among several others.

There has been significant attention on extracting medium attenuation from surface waves due to seismic noise [*Prieto et al.*, 2009; *Weaver*, 2011; *Lin et al.*, 2012; *Zhang and Yang*, 2013], as this has direct implications in propagation modeling and earthquake ground motion predictions [*Roux et al.*, 2005a; *Prieto and Beroza*, 2008; *Denolle et al.*, 2013, 2014]. The spatial coherence of noise has been used to estimate the attenuation coefficient by modeling the attenuation as an exponential decay of the coherence with distance [*Matzel*, 2008; *Prieto et al.*, 2009; *Weemstra et al.*, 2013] and maps of attenuation across the western United States inferred using this approach have been published [*Lawrence and Prieto*, 2011]. Several analytical and numerical studies [*Cupillard and Capdeville*, 2010; *Tsai*, 2011; *Weaver*, 2011; *Nakahara*, 2012; *Walker*, 2012; *Walker and Buckingham*, 2012; *Liu and Ben-Zion*, 2013] indicate that the recovery of the attenuation depends strongly on the directionality of noise sources and that the exponential decay model is valid only under restricted assumptions. However, *Lawrence et al.* [2013] numerically evaluate the spatial coherence under different noise directionalities and distributions and showed that the estimated attenuation supports the exponential decay model. The debate over the interpretation of amplitude (and the feasibility of extracting

reliable estimates) is a reflection of the inherent challenges in estimating attenuation such as the noise directionality, slowness inhomogeneity, site amplification factors, and focusing and defocusing effects, all of which influence the amplitude.

Averaging, which is ubiquitous in ambient noise processing, often is used to obtain reliable estimates [*Bensen et al.*, 2007] or to bring the distribution of noise sources closer to isotropic [*Asten*, 2006; *Prieto et al.*, 2009] or to homogenize the medium properties. Depending on the quantity being averaged and the assumptions made about the environment (which might not hold true in data), this could result in biased or altogether incorrect results. For example, the Southern California region is modeled as a laterally homogeneous dispersive medium, but in reality it has regions with sharp slowness contrasts, such as the Los Angeles and Ventura basins, and averaging certain quantities in such a scenario could be a source of mismatch between the model and estimates from data [*Weaver*, 2011]. In this article we investigate the role played by factors such as the processing, array geometry and the inhomogeneity of the environment on the spatial coherence and discuss whether attenuation can be retrieved reliably from the coherence using the approach put forth in *Prieto et al.* [2009]. These factors typically are ignored in analytical and numerical work to aid tractability but indeed play a significant role when working with actual seismic data.

We show that performing certain common preprocessing steps, such as averaging neighboring frequencies (section 3.4), is sufficient to introduce attenuation-like effects in the coherence. In addition, since the ambient noise field typically is composed of higher-mode Rayleigh waves and *P* waves (section 5), the actual form of the estimated coherence is markedly different from idealized theoretical models (section 6), and the differences between the two also could be interpreted as attenuation. Finally, in section 8, we discuss the attenuation-like effects arising from using the coherence-based processing in an inhomogeneous medium.

2. Background

2.1. Spatial Coherence Functions

The spatial coherence function (SCF) of a noise field describes the correlations between the response at two stations in the frequency domain (the SCF is also known as the spatial autocorrelation function or SPAC, following *Aki* [1957]). Consider seismic surface waves at a frequency f, with a normalized azimuthal weight function $W(\theta)$, incident on two stations A and B positioned r apart with an interstation azimuth of ζ in a homogeneous medium. From the complex valued signals $\psi_A(f)$ and $\psi_B(f)$ recorded, the cross-spectral density (CSD) is given by

$$P_{AB}(f) = \tau^{-1}\langle \psi_A(f)\psi_B^*(f)\rangle, \tag{1}$$

where τ denotes the observation time, $*$ the complex conjugate, and $\langle\cdot\rangle$ the ensemble average. The SCF between these two sensors is defined as the normalized cross-spectral density,

$$\Gamma(r,\zeta) = \frac{P_{AB}(f)}{\sqrt{P_{AA}(f)P_{BB}(f)}}, \tag{2}$$

where $P_{AA}(f) = \tau^{-1}\langle \psi_A(f)\psi_A^*(f)\rangle$ and $P_{BB}(f) = \tau^{-1}\langle \psi_B(f)\psi_B^*(f)\rangle$ are the respective power spectral densities.

Following *Cox* [1973, equation (19)], the SCF for a given noise distribution $W(\theta)$ is obtained by integrating over all azimuths, as follows:

$$\begin{aligned}\Gamma_{2\text{-D}}(r,\zeta) &= \frac{1}{2\pi}\int_0^{2\pi} W(\theta)\exp\left(\iota 2\pi fr\cos(\theta-\zeta)s\right)\mathrm{d}\theta \\ &= \sum_{\nu=0}^{\infty} \iota^{\nu}\epsilon_{\nu}\mathrm{J}_{\nu}(2\pi frs)[a_{\nu}\cos(\nu\zeta) + b_{\nu}\sin(\nu\zeta)]\end{aligned} \tag{3}$$

where s is the frequency-dependent slowness of the medium, the Neumann factor ϵ_{ν} is 1 for $\nu = 0$ and 2 otherwise, and a_{ν}, b_{ν} are the Fourier coefficients of $W(\theta)$. Thus, for arbitrary noise fields, the SCF depends on the interstation azimuth ζ. When the noise field is isotropic, then $W(\theta) = 1$ and only the $\nu = 0$ term is nonzero, and the SCF is [*Aki*, 1957]

$$\Gamma_{2\text{-D}}(r) = \mathrm{J}_0(2\pi frs); \tag{4}$$

i.e., it is independent of the interstation azimuth ζ and is simply a function of the frequency f and the separation distance r.

For body waves, which propagate three dimensionally, the SCF for a noise distribution $W(\theta, \phi)$ is given by *Cox* [1973, equation (43)],

$$\begin{aligned}\Gamma_{3\text{-}D}(r,\zeta,\xi) &= \frac{1}{4\pi}\int_0^{2\pi}\int_0^{\pi} W(\theta,\phi)\sin(\theta)\exp\left[\imath 2\pi frs\right.\\ &\quad\left.\times\left(\sin(\theta)\sin(\xi)\cos(\phi-\zeta)+\cos(\theta)\cos(\xi)\right)\right]\mathrm{d}\theta\,\mathrm{d}\phi\\ &= \sum_{n=0}^{\infty}\sum_{m=0}^{\infty}\imath^n P_n^m(\cos(\xi))j_n(2\pi frs)\left[a_n^m\cos(m\xi)+b_n^m\sin(m\xi)\right]\end{aligned} \tag{5}$$

where ξ is the interstation angle from the z axis, P_n^m is the associated Legendre function of the first kind, order m and degree n, a_n^m and b_n^m are the coefficients in the spherical harmonic expansion of $W(\theta, \phi)$, and j_n is the spherical Bessel function of order n. When the noise field is isotropic, then $W(\theta, \phi) = 1$, and only the $n = 0$ term remains, and the SCF is $\Gamma_{3\text{-}D} = j_0(2\pi frs)$ [*Eckart*, 1953] (or sinc).

Attenuation in the coherence often is modeled as a multiplicative term, $g(\alpha, r)$ where α is the attenuation coefficient. The form of $g(\alpha, r)$ must be known in order to interpret it [*Tsai*, 2011]. Much of the theoretical work has focused on the analytical form of $g(\alpha, r)$ [*Tsai*, 2011; *Nakahara*, 2012; *Walker*, 2012] which needs to be known before interpreting α in terms of the surface wave quality factor Q. A common choice is to assume $g(\alpha, r) = e^{-\alpha r}$ [*Prieto et al.*, 2009], which is approximately valid for small attenuation [*Nakahara*, 2012].

2.2. Estimating the SCF From Seismic Arrays

In general, the seismic ambient noise field is not isotropic, and the observed coherence between station pairs depends on the distribution of noise sources [*Cox*, 1973; *Tsai*, 2011]. High-density seismic networks such as the Southern California Seismic Network (SCSN) have several station pairs of varying interstation azimuths and distances (over 10,000 pairs for SCSN). It then is possible to leverage the multitude of pairs available at a certain distance of separation to mitigate the effect of the directionality of the noise field, at the cost of assuming uniform medium properties for the entire study region.

Prieto et al. [2009] suggested averaging the observed coherence for multiple station pairs at a fixed separation distance, to approximate an isotropic noise distribution. Mathematically, this can be seen by integrating (3) over all station pair azimuths (ζ from 0 to 2π). Regardless of the noise distribution $W(\theta)$, only the $\nu = 0$ term remains.

From the observed interstation coherencies $\hat{\Gamma}(r_{ij}, \zeta_{ij})$, the "average spatial coherence" (ASC) for the array is obtained by binning the observations into Δ_d wide bins and averaging them [*Prieto et al.*, 2009]. The average coherence $\tilde{\Gamma}_n$ for the nth distance bin d_n is obtained as

$$\tilde{\Gamma}_n = \Re\left\langle\hat{\Gamma}(r_{ij},\zeta_{ij})\right\rangle\ \forall(i,j)\in\mathcal{D}_n \tag{6}$$

where $\mathcal{D}_n = \{(i,j)\,|\,d_n \le r_{ij} < d_{n+1}\}$ is the set of station pairs in the nth distance bin and $\Re$ denotes the real component. The imaginary part of the ASC is zero for a symmetric $W(\theta)$, and the averaging reduces the imaginary part [*Asten*, 2006; *Prieto et al.*, 2009], thus justifying the use of only the real part.

3. Data and Signal Processing

3.1. Preprocessing

Data recorded on broadband seismic stations in Southern California (Figure 1) were collected for the entire year of 2007 at a sampling rate of 1 Hz. We use only the vertical component data in the 0.05–0.2 Hz frequency range. After removing instrument glitches in the raw data, the data were divided into segments of 1800 s each (30 min), windowed with a Blackman-Harris window, and Fourier transformed with a 2048 point fast Fourier transform. The resulting vector of Fourier coefficients (for all stations) at each frequency and segment m is referred to as a "snapshot" $\mathbf{x}_m = [x_{m1}, \cdots, x_{mN}]^T$, where N is the number of stations.

Earthquakes and other teleseismic events tend to skew the results in noise processing due to their disproportionate power compared to the background noise field. We remove outliers in the data by computing the median of the snapshot power across a 24 h sliding window for each frequency and discarding snapshots that have powers that are more than 1.5 median absolute deviations away from the median [*Huber*,

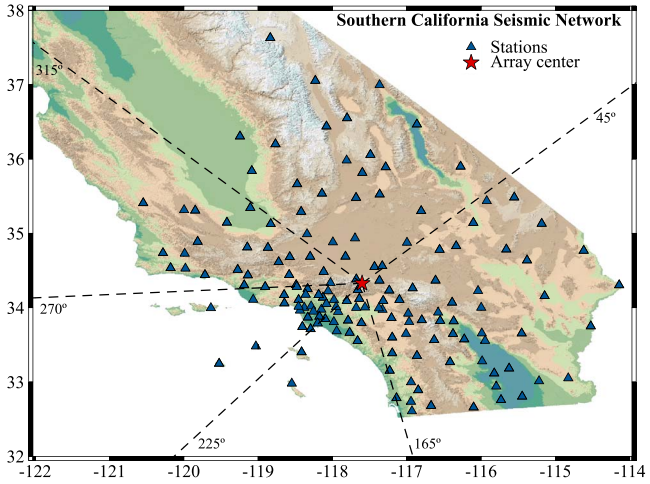

Figure 1. Stations in the Southern California Seismic Network and key azimuths (dashed) from the center of the array.

1981]. This approach has similarities to time domain techniques that use the ratio of the peak amplitude to the root mean square amplitude as a rejection criterion [*Bensen et al.*, 2007]. We do not perform any additional temporal or frequency domain truncations or normalizations such as 1 bit processing [*Larose et al.*, 2004] or spectral whitening.

3.2. Normalized Cross-Spectral Density Matrix

The spatial covariance matrix or the cross-spectral density matrix from M observations of the N dimensional snapshot vector $\mathbf{x}_m$ is defined as

$$\hat{\Sigma} = \frac{1}{M}\sum_{m=1}^{M} \mathbf{x}_m \mathbf{x}_m^H. \tag{7}$$

where H denotes Hermitian transpose. In general, due to site amplification factors or differences in sensor characteristics, the powers at different sensors are not identical. The normalized cross-spectral density matrix (CSDM) is

$$\hat{\Sigma}' = \chi \hat{\Sigma} \chi^T, \tag{8}$$

where $\chi = \mathrm{diag}\left(\left[\frac{1}{\sqrt{\hat{\Sigma}_{11}}}, \cdots, \frac{1}{\sqrt{\hat{\Sigma}_{NN}}}\right]\right)$, is a diagonal matrix. This normalization reduces the influence of site amplification factors.

We compute the CSDM for each month, using the snapshots that satisfy the criteria in section 3.1. With the normalization in (8), the ijth element of the CSDM gives an M sample estimate of the coherence between the ith and jth station pair as in (2).

3.3. Capon Beamforming

For a given frequency f, azimuth θ, and slowness s, the array manifold vector $\mathbf{v}(\theta, s)$ is given by

$$\mathbf{v}(\theta, s) = \frac{1}{\sqrt{N}} e^{\imath 2\pi f \mathbf{p}_\theta s} \tag{9}$$

where $\mathbf{p}_\theta = [\mathbf{r}_1 \cdot \mathbf{u}_\theta, \ldots, \mathbf{r}_N \cdot \mathbf{u}_\theta]^T$ is the projection vector, $\mathbf{r}_i$ is the position vector of the ith station (with the origin at the mean latitude and longitude), and $\mathbf{u}_\theta$ is the unit vector along θ.

The weight vector $\mathbf{w}(\theta, s)$ for the Capon beamformer [*Capon*, 1969] (or the minimum variance distortionless response beamformer) is constrained to have unit gain in the look direction, while at the same time minimizing the output power, thus leading to the optimal weights

$$\mathbf{w}_{\mathrm{mvdr}}(\theta, s) = \frac{\hat{\Sigma}'^{-1}\mathbf{v}(\theta, s)}{\mathbf{v}^H(\theta, s)\hat{\Sigma}'^{-1}\mathbf{v}(\theta, s)} \tag{10}$$

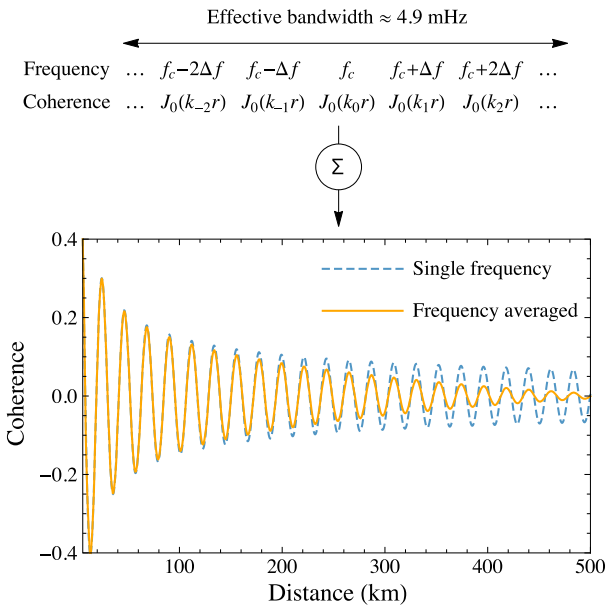

Figure 2. Spatial coherence at 0.14 Hz with and without frequency averaging.

If $\hat{\Sigma}'^{-1}$ is not invertible (for noise processing, $M > N$, and $\hat{\Sigma}'$ often is invertible due to uncorrelated noise), then the matrix can be made full rank by loading the diagonal to constrain the white noise gain [*van Trees*, 2002]. In comparison, the weights for the conventional beamformer are given by $\mathbf{w}_{\text{conv}}(\theta, s) = \mathbf{v}(\theta, s)$. The beamformer outputs then are given by

$$B_{(\cdot)} = \mathbf{w}_{(\cdot)}^H \hat{\Sigma}' \mathbf{w}_{(\cdot)} \tag{11}$$

3.4. Interference Due to Frequency Averaging

It is not uncommon in signal processing to average $\hat{\Sigma}'$ (or the coherences) across neighboring frequency bins to get a robust estimate. Although this is desirable in certain applications, here such an averaging will introduce attenuation-like effects in the coherence due to interference from different wave numbers ($k = 2\pi fs$) associated with each frequency bin.

For example, consider isotropic surface noise with a uniform power spectrum in a lossless laterally homogeneous medium. Using a sampling frequency of 1 Hz and an FFT length of 2048 points, the bin width is $\Delta f \approx 0.49$ mHz. Averaging 10 bins centered at $f_c \approx 0.14$ Hz (effective bandwidth of ≈ 4.9 mHz) using the slowness dispersion in section 5.1 results in an SCF

$$\Gamma_{f\text{avg}} = \frac{1}{10} \sum_{f=f_c-5\Delta f}^{f_c+4\Delta f} \mathrm{J}_0\left(2\pi f s(f) r\right) \tag{12}$$

that has an apparent attenuation (Figure 2). Due to the dependence of the wave number on frequency, this effect will always be present, even in a nondispersive medium.

The actual effects of such an averaging in data also will depend on the noise power spectrum and the weighting used, and it is preferable to minimize frequency averaging. If performed, the apparent attenuation should be considered when interpreting the results.

4. Influence of the Array Geometry

Factors independent of the noise field or the environment such as limitations imposed by the array geometry and artifacts from data processing can affect the estimate of the coherence. Understanding these issues is beneficial in the interpretation of the coherence estimates in section 6.

4.1. Diminishing Number of Station Pairs With Distance

Figure 3a shows a smoothed 2-D histogram of the station pairs density along distance and azimuth for the entire SCSN. The predominantly SE-NW orientation of the interstation azimuths (arising due to the layout of the stations along the Bight) is evident from the higher density of station pairs between 80 and 140°. The distribution is symmetric, so only 0–180° is shown. The distribution becomes thin beyond about 400 km, occupying progressively fewer azimuths.

It is useful to have a simple rule of thumb for selecting the range in which the ASC is well estimated. This can be derived intuitively for random regional arrays such as the SCSN. Assuming the stations are normally distributed in range in all directions around the mean latitude and longitude (around 34°N, 117°W for the SCSN), then the number of station pairs with distance is Rayleigh distributed. The raypath distribution for the SCSN (solid) is shown in Figure 3b, and it resembles a Rayleigh distribution with its mode at

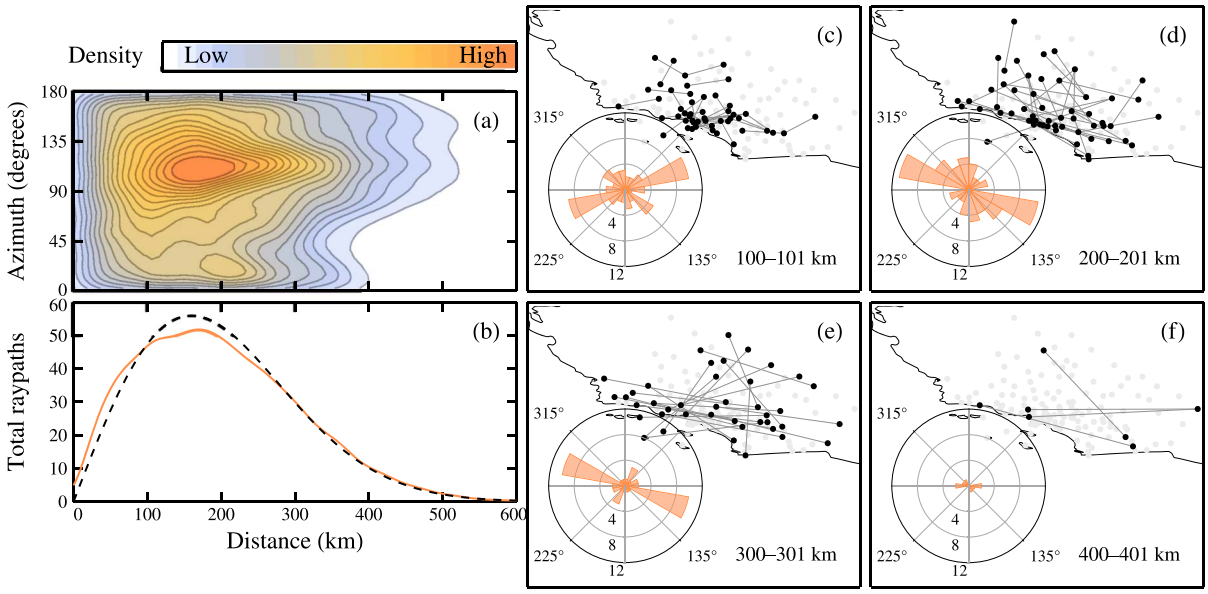

Figure 3. (a) Smoothed 2-D histogram of the interstation distances and azimuths. (b) Raypath histogram with distance (solid) approximated by a Rayleigh distribution (dashed). (c–f) Interstation azimuthal distribution (sector chart) at certain distance bins. The station pairs that are present in each bin are shown by the connected station pairs.

about 160 km (the deviation is explained by the higher station density in the Los Angeles basin thus having shorter paths).

From the histograms in Figures 3a and 3b, it is likely that the ASC is better estimated between about 20 and 400 km (over 10 station pairs in each bin) and bins outside this range generally provide noisy estimates. Hence, we only use the ASC within this range in section 6.

4.2. Uneven Azimuthal Distribution of Station Pairs

Figures 3c–3f show the distribution of the interstation azimuths (every 15°) at different distance bins (sector plots) and the station pairs that belong to each bin. While in principle (6) amounts to an azimuthal average across all station pairs in that bin, this average is weighted more along NW-SE for the SCSN because of the layout of the array (this will vary depending on the array). The potential bias arising from overweighting along certain azimuths due to the increased number of station pairs (see the increased density of stations between 90 and 135° azimuth in Figure 3a and also excess paths along 250° in Figures 3c and 3e and along 280–315° in 3d) can be reduced by implementing an azimuthal binning.

We bin the station pairs in $\mathcal{D}_n$ into Δ_θ wide azimuth bins, compute the mean in each range bin, and then azimuthally average the means, in order to ensure a more equal weighting from all azimuths. The ASC then is given by

$$\tilde{\Gamma}'_n = \Re\left\langle \sum_l \frac{1}{\#\mathcal{A}_{\mathrm{ln}}} \hat{\Gamma}(r_{ij},\zeta_{ij}),\ (i,j) \right\rangle \forall \in \mathcal{A}_{\mathrm{ln}} \tag{13}$$

where $\mathcal{A}_{\mathrm{ln}} = \{(i,j)\,|\,\theta_l \le \zeta_{ij} < \theta_{l+1}, (i,j) \in \mathcal{D}_n\}$ is the set of station pairs that are in the nth distance bin and lth azimuth bin θ_l, and # denotes cardinality of the set (empty sets are not considered). The ASC $\tilde{\Gamma}'$ is estimated by substituting $\hat{\Gamma}(r_{ij},\zeta_{ij}) = \hat{\Sigma}'_{ij}$ in (13).

Equations (6) and (13) are identical when each azimuth has the same number of interstation pairs. However, a drawback of (13) is that it ignores the variances at different azimuths (as does (6)), since the noise distribution and the inhomogeneity in the region are unknown. In other words, it weighs azimuth bins with just a single path (poorly estimated) the same as bins with a large number of station pairs (well estimate) (e.g., see azimuthal distribution of station pairs for 300–301 km in Figure 3e).

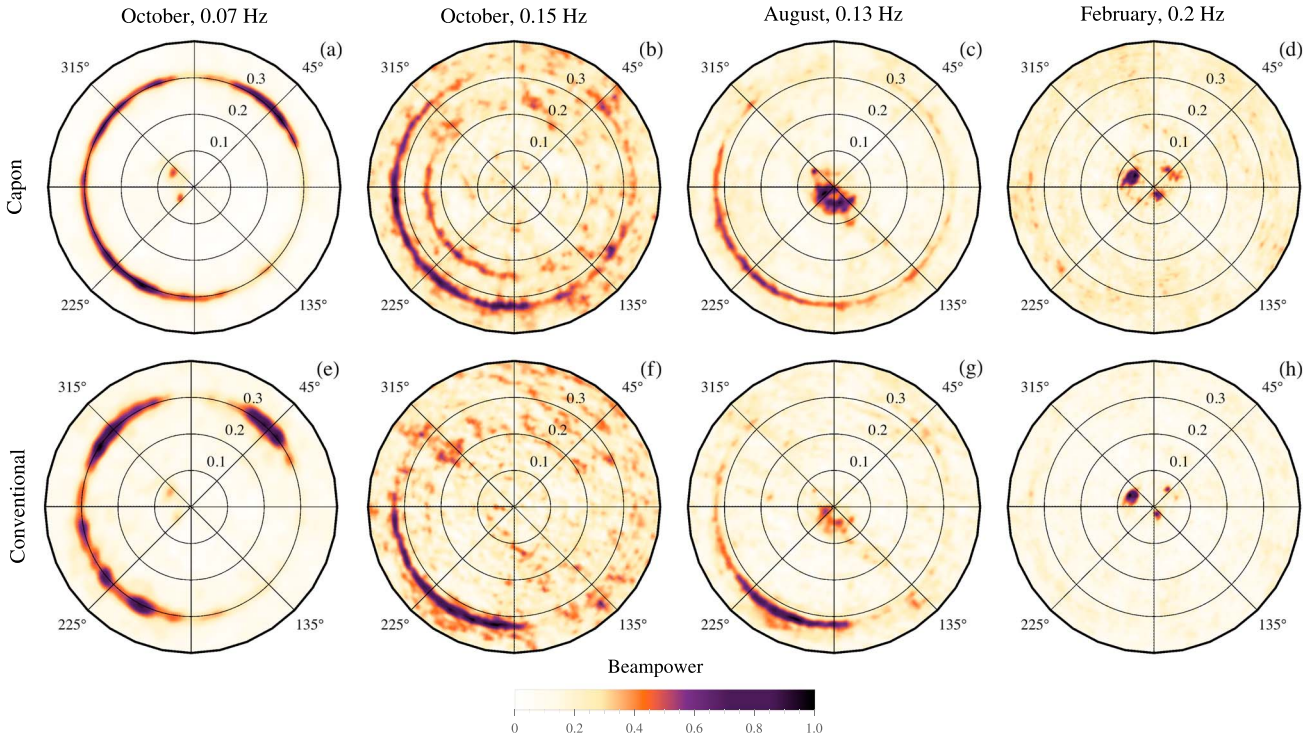

Figure 4. (a–d) Capon beamformer outputs for different months and frequencies normalized by the maximum in each panel. The first mode of the surface Rayleigh wave, $\mathcal{R}_1$, is seen between 0.12 and 0.2 Hz in Figure 4b. (e–h) Conventional beamformer outputs for the same month and frequencies as in Figures 4a–4d.

5. Composition of the Ambient Seismic Noise Field

Excitation of Rayleigh waves in a laterally homogeneous medium (variations only in depth) generates higher modes in addition to the fundamental, with the frequency-phase speed relationship given by the dispersion equation. Barring a few exceptions [*Haubrich and McCamy*, 1969; *Harmon et al.*, 2007; *Nishida et al.*, 2008; *Brooks et al.*, 2009], most studies using seismic noise only retrieve the dominant fundamental mode Rayleigh wave. *P* waves have also been observed in the microseism frequency band and originate from deep water storms [*Haubrich and McCamy*, 1969; *Gerstoft et al.*, 2006b, 2008; *Zhang et al.*, 2010; *Gualtieri et al.*, 2014] (slowness below 0.1 s/km) and local meteorological forcing [*Roux et al.*, 2005b] (slowness around 0.19 s/km).

Capon and conventional beamformer outputs are shown at different frequencies and months in Figure 4 (the beamforming is performed by discretizing the θ-s space every 1° from 0 to 360° in the azimuth and every 0.0025 s/km from 0 to 0.4 s/km slowness). The frequencies and months were chosen to highlight different aspects of the seismic noise field, namely,

1. Microseismic noise that propagates as fundamental mode Rayleigh wave ($\mathcal{R}_0$) and appear predominantly from the west (Figures 4a–4c, between 0.3 and 0.33 s/km slowness) [*Gerstoft and Tanimoto*, 2007].
2. First-mode Rayleigh wave ($\mathcal{R}_1$), usually seen between 0.12 and 0.2 Hz (Figure 4b at about 0.23 s/km slowness). Due to the lower resolution of the conventional beamformer, the higher mode is not easily observable.
3. Body waves from distant storms [*Zhang et al.*, 2010] and $\mathcal{R}_0$ (and often $\mathcal{R}_1$) (Figure 4c at $<$ 0.1 s/km slowness).
4. Dominant body waves from storms at the higher end of the microseism band (Figure 4h).

These waves are present at predictable times and frequencies, showing that the seismic noise field is composed of much more than just $\mathcal{R}_0$. Although some of the results in this section are available in existing literature, we analyze and discuss them in detail for this specific data set, which forms the basis for the discussion in section 6.

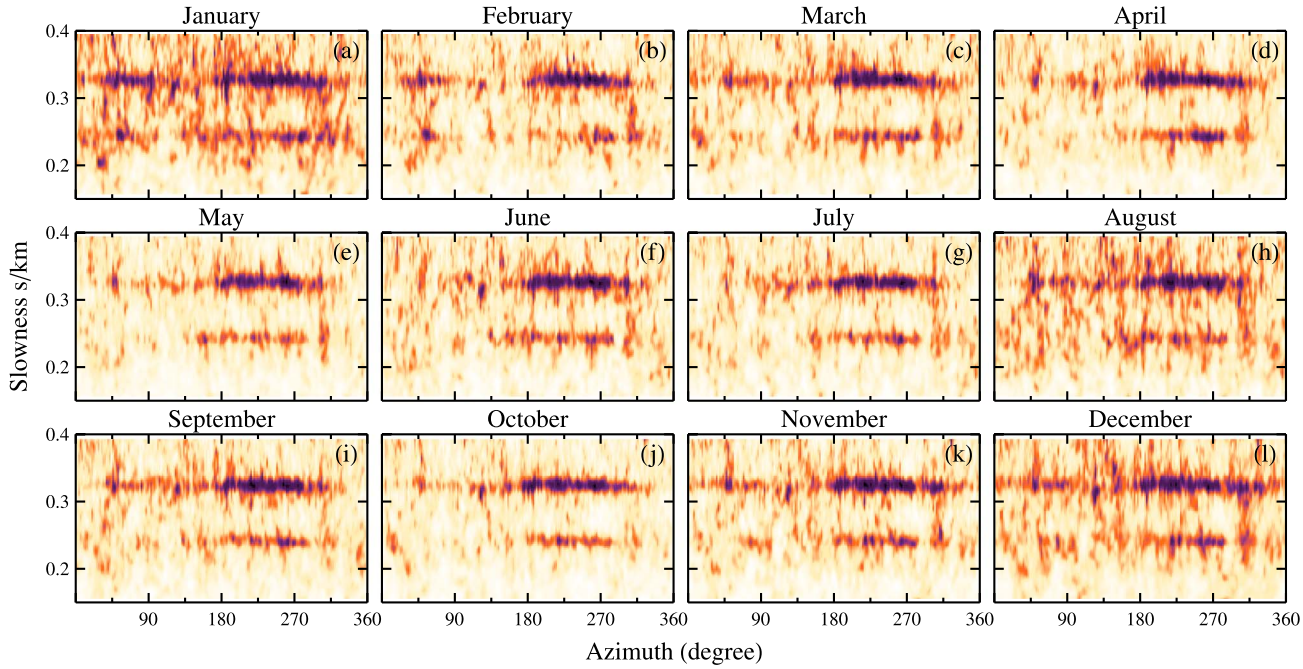

Figure 5. Capon beamformer outputs at 0.15 Hz between 0.15 and 0.4 s/km slowness for all months in 2007 (each subplot is normalized by its maximum). The color scale is the same as in Figure 4.

5.1. Fundamental and Higher-Mode Rayleigh Waves

Figure 5 shows the Capon beamformer output for all months in 2007 between 0.15 and 0.4 s/km slowness. The $\mathcal{R}_1$ wave is observed consistently at 0.24 s/km slowness, alongside the $\mathcal{R}_0$ at 0.32 s/km. The generating regions of $\mathcal{R}_1$ are confined to a smaller azimuthal region to the west of the array than $\mathcal{R}_0$. They are observed at other azimuths when accompanied by powerful storms such as those in the Labrador Sea and North Atlantic Ocean in the winter months (see 30–60° in Figures 5a and 5b), or hurricanes in the Gulf of Mexico and the Atlantic Ocean (see 60–120° in Figure 5h). $\mathcal{R}_1$ especially is illuminated strongly at certain specific azimuths (see azimuths 270° and 315° in Figures 5a–5f and 250° in Figures 5c, 5d, 5f, and 5k). However, note that the array is more coherent in the sedimentary basins due to the high density of stations, and it is quite likely that this mode is supported only in these regions, although the origins of the mode are beyond the scope of this paper.

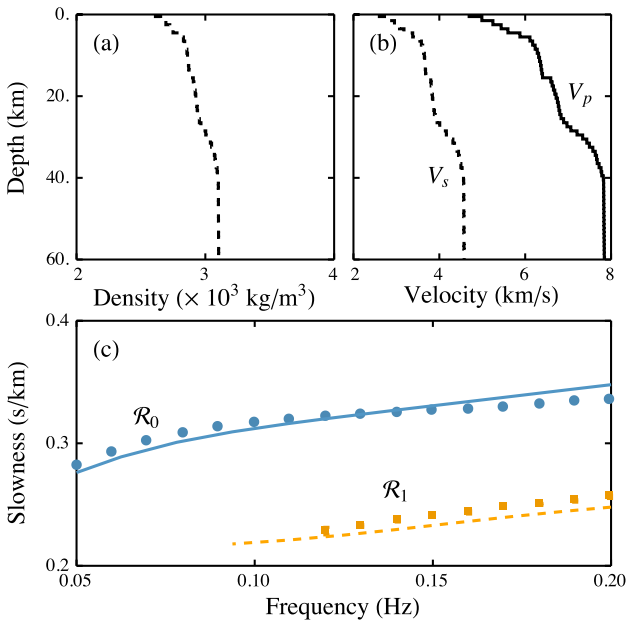

Figure 6. (a) Density and (b) compressional and shear velocity profiles for Southern California obtained by averaging the respective quantities at all station locations. (c) Average slowness estimates for $\mathcal{R}_0$ (circles), $\mathcal{R}_1$ (squares), and the dispersion curves computed using the model in Figure 6b.

The phase slownesses of the two modes are estimated and compared against the simulated dispersion curves in Figure 6. For the simulation, velocity and density profiles are obtained at each of the station locations [*Kohler et al.*, 2003] (sampled every 1 km in depth through 60 km) and averaged to obtain a "mean velocity model" for

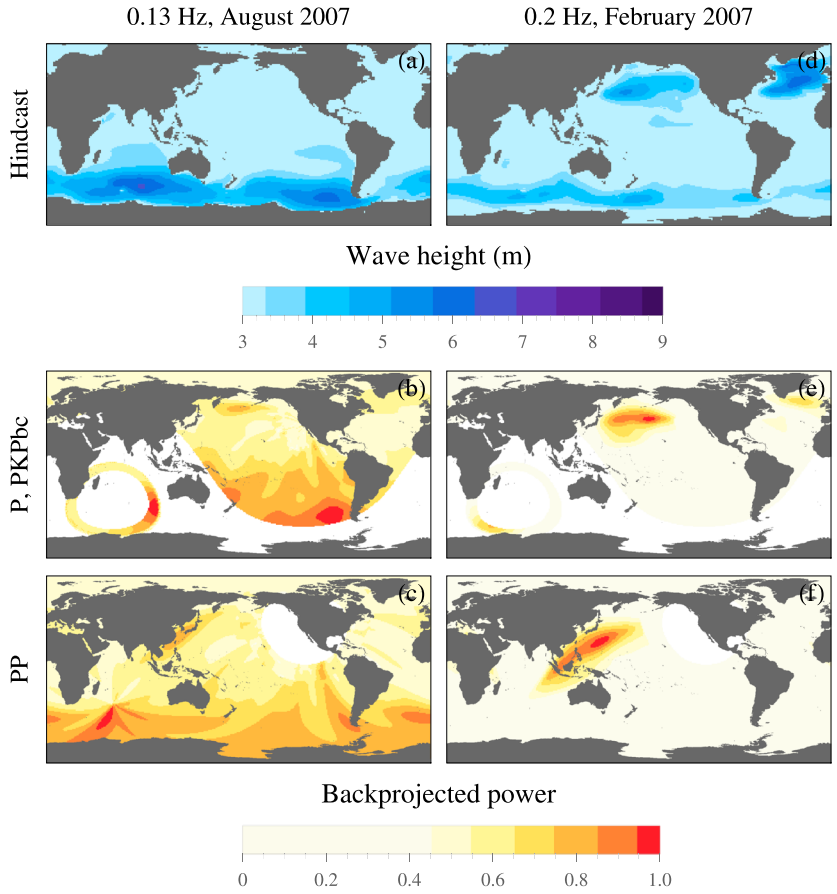

Figure 7. Mean ocean wave height for August 2007 and (b and c) body wave backprojections for the P, PP, and PKPbc phases at 0.13 Hz. (d–f) same as in Figures 7a–7c, at 0.2 Hz in February.

Southern California (see Figures 6a and 6b for the resulting model). The resulting slowness dispersion curves [*Hermann*, 2010] for the first two modes are shown by the lines in Figure 6c.

The observed phase slownesses (averaged over the region of study) are obtained from the beamformer output by averaging across all azimuths and searching for the maximum in a restricted slowness space (here 0.27–0.4 s/km for the dominant mode $\mathcal{R}_0$) as [*Harmon et al.*, 2008]

$$\hat{s}_{\mathcal{R}_0} = \underset{s}{\operatorname{argmax}} \langle B(\theta, s) \rangle_\theta \,,\ 0.27 \le s \le 0.4,\ f \in [0.05, 0.2] \tag{14}$$

The $\mathcal{R}_0$ phase slownesses (medians shown by circles in Figure 6c) are very consistent across different months.

Since $\mathcal{R}_1$ is present only in the 0.12–0.2 Hz band, its slowness can be estimated as in (14) but by further restricting the search space to exclude the fundamental mode:

$$\hat{s}_{\mathcal{R}_1} = \underset{s}{\operatorname{argmax}} \langle B(\theta, s) \rangle_\theta \,,\ 0.2 \le s \le s_{\max},\ f \in [0.12, 0.2] \tag{15}$$

where $s_{\max}$ is either a sufficiently large value (here 0.27 s/km) or a frequency-dependent value such as $s_{\max} = f/3 + 3/14$ (based on the simulated dispersion curve). Both approaches give identical results (squares in Figure 6).

The estimated slownesses for both modes agree very well with the simulated dispersion curves. The dispersion of the fundamental and higher modes can be used to estimate the shear wave velocity with depth for the region.

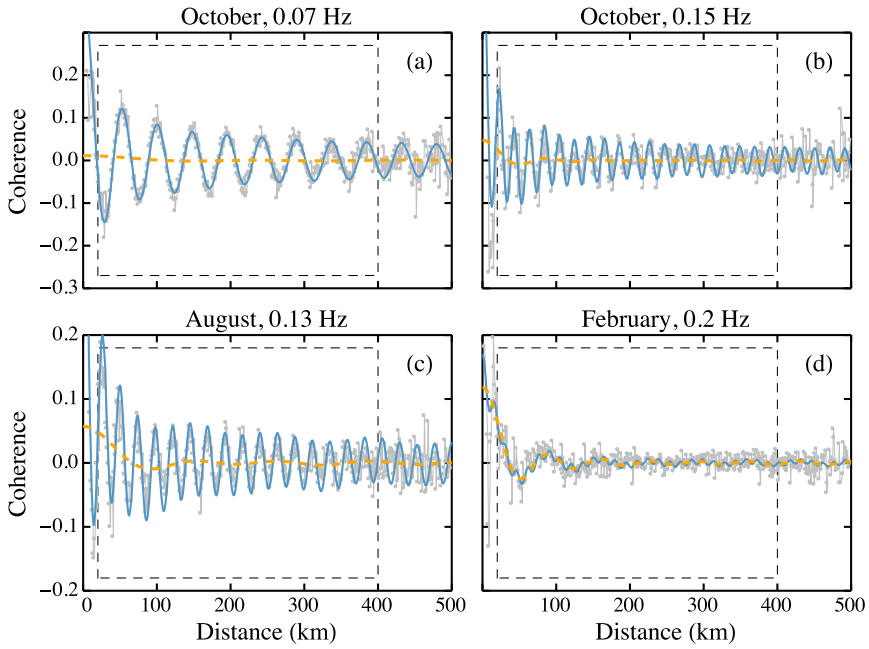

Figure 8. Observed ASC (circles, thin gray lines) for different months and frequencies and the best fit SCF (solid, blue) obtained from (17). The fit was computed only between 20 and 400 km (rectangle) due to insufficient station pairs at shorter and longer distances (see section 4.1). The contribution of the *P* waves to the SCF is shown by dashed lines.

5.2. Body Waves From Distant Storms

The body wave arrivals seen in Figures 4c and 4d are backprojected assuming a grid of sources and traveltime tables [*Kennett et al.*, 1995] corresponding to an assumed propagation path (P, PP, etc.) [*Gerstoft et al.*, 2008]. The high-energy regions in the backprojected maps in Figure 7 (P, PP, and PKPbc) correspond well with the respective hindcasts. Specifically, note the absence of strong *P* waves from an 8.0 *Mw* earthquake in Peru (15 August 2007) in Figures 7b and 7c which was removed in the outlier rejection (section 3.1), indicating that the energy observed is mostly from storms in the Southern Ocean.

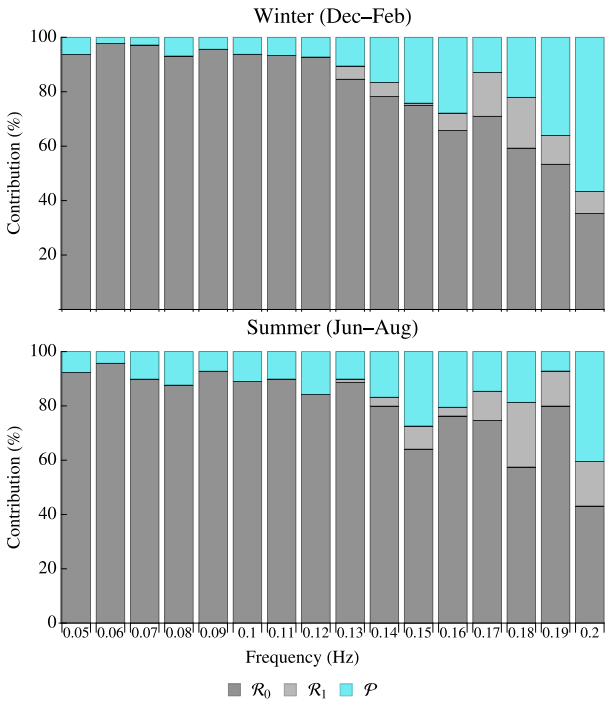

Figure 9. Contribution of $\mathcal{R}_0$, $\mathcal{R}_1$, and body waves to the SCF, averaged over the Northern Hemisphere winter (December–February) and summer (June–August) months.

The body wave energy is strongest above 0.16 Hz [*Zhang et al.*, 2010], but it is seen throughout the 0.12–0.2 Hz band. In February, the body waves in the 0.17–0.2 Hz band primarily are from storms in the NW Pacific (Figures 7d–7f show the hindcast and backprojections at 0.2 Hz) whereas body waves from the Atlantic storms are observed at lower frequencies (0.16–0.18 Hz), not shown here. In comparison, the storms from the Southern Ocean are observed throughout the frequency band of interest.

6. Observed Spatial Coherence

Following the analysis in section 5, it is clear that the ambient seismic noise field

in Southern California contains (in the microseism band) $\mathcal{R}_0$ and $\mathcal{R}_1$ Rayleigh waves, and body waves from distant storms. It stands to reason that the estimated ASC will be influenced by these waves, possibly in undesirable ways, and thus must be taken into consideration.

The ASC $\tilde{\Gamma}$ is obtained as in (13) with $\Delta_d = 1$ km and $\Delta_\theta = 15°$ (Figure 8). To avoid insufficient averaging in each bin, we compute the ASC only for those distance bins that have at least 10 station pairs (i.e., $\#\mathcal{D}_n \geq 10$). For the entire SCSN this covers the distance bins between approximately 20 and 400 km (section 4.1).

6.1. Multipath Effects on the ASC

The presence of multiple-propagation paths at each frequency (even without considering the effects of scattering) suggests that the underlying SCF might be better modeled as a superposition of 2-D surface (including higher modes) and 3-D body waves of different slownesses, rather than only the fundamental mode Rayleigh wave. The noise distribution for body waves will not be isotropic even after azimuthal averaging (because all the noise is from below the array and includes waves reflecting from interfaces). For the purposes of this discussion, we only use the first term (5) corresponding to $n = m = 0$ and estimate the weight or the coefficient a_0^0 numerically. Thus, the model SCF $\Gamma_{\text{model}}(r)$ is

$$\Gamma_{\text{model}}(r) = \sum_{m\in\mathcal{R}} q_m \mathrm{J}_0(2\pi f s_m r) + \sum_{p\in\mathcal{P}} q_p j_0(2\pi f s_p r) \tag{16}$$

where q_m and q_p indicate the relative contribution of the component to the SCF, $\mathcal{R}$ denotes the different Rayleigh wave modes (here $\mathcal{R}_0$ and $\mathcal{R}_1$), and $\mathcal{P}$ denotes the different body wave phases. Note that q_m and q_p values only indicate the contributions as observed by the SCSN array for noise in the Southern California region and will be different for a different array and region.

Using the estimates $\hat{s}_{\mathcal{R}_0}$ in (14) and $\hat{s}_{\mathcal{R}_1}$ in (15), we estimate q_m, q_p, and $s^{(p)}$ in (16) from the ASC by the following minimization using an exhaustive search:

$$\underset{\substack{q_{\mathcal{R}_0},q_{\mathcal{R}_1}\\ q_{\mathcal{P}_1},q_{\mathcal{P}_2}\\ s_{\mathcal{P}_1},s_{\mathcal{P}_2}}}{\operatorname{argmin}} \sum_n \left| \tilde{\Gamma}'_n - \sum_{m=\mathcal{R}_0,\mathcal{R}_1} q_m \mathrm{J}_0\left(2\pi f \hat{s}_m d_n\right) - \sum_{p=\mathcal{P}_1,\mathcal{P}_2} q_p j_0\left(2\pi f s_p d_n\right) \right| \tag{17}$$

where $s_{\mathcal{P}_1}$ and $s_{\mathcal{P}_2}$ are constrained to be between 0 and 0.1 s/km and the ℓ_1 norm is used to reduce the impact of outliers in the data (the summation is over all the distance bins). We only search for at most two body wave phases (any of P, PP, or PKP) since there are usually around zero to two distinct regions in the backprojection. The number of $\mathcal{P}$ components can be increased appropriately based on the number of peaks below 0.1 s/km in the corresponding beamformer output but is not done here.

The best fit SCF $\hat{\Gamma}^{(\text{model})}$ then is obtained by substituting the estimated quantities in (16) and is shown in Figure 8 for the same frequencies and months considered in Figure 4. The multicomponent SCF model in (16) captures closely the weak "beating" effects in the ASC (clearly seen in Figure 8c) arising due to the interference between the different wave numbers corresponding to different propagation paths ($\mathcal{R}_0$ and $\mathcal{R}_1$ have the same raypath but propagate at different wave speeds.). While for most purposes a simple $\mathcal{R}_0$ only model might suffice, the results here show that contributions from additional wave numbers can cause phase cancelation effects which could influence the estimation of the attenuation.

The contribution from the body waves is shown by the dashed lines which captures the long-wavelength fluctuations of the ASC (Figure 8c). The impact of *P* wave microseisms is more pronounced on the ASC at higher frequencies, especially in the winter months (December–February), when the body waves primarily originate from large storms in the West Pacific and North Atlantic. The resulting ASC (Figure 8d) resembles a sinc more than a Bessel function (from the estimated relative contributions, 67% of the SCF is due to body waves).

6.2. Composition of the SCF

The composition of the multicomponent SCF as observed by the SCSN array using (17) also varies with season and frequency. From the estimated $\hat{q}$ values, we compute the percentages of $\mathcal{R}_1$, $\mathcal{R}_2$, and $\mathcal{P}$ (combined) and the relationship between them for the summer (June–August) and winter (December–February) months as shown in Figure 9.

At the lower end of the microseism band (primary microseisms), $\mathcal{R}_1$ is not observed and the SCF is dominated by $\mathcal{R}_0$ in both seasons. Modest contributions from body waves are occasionally observed (such as the

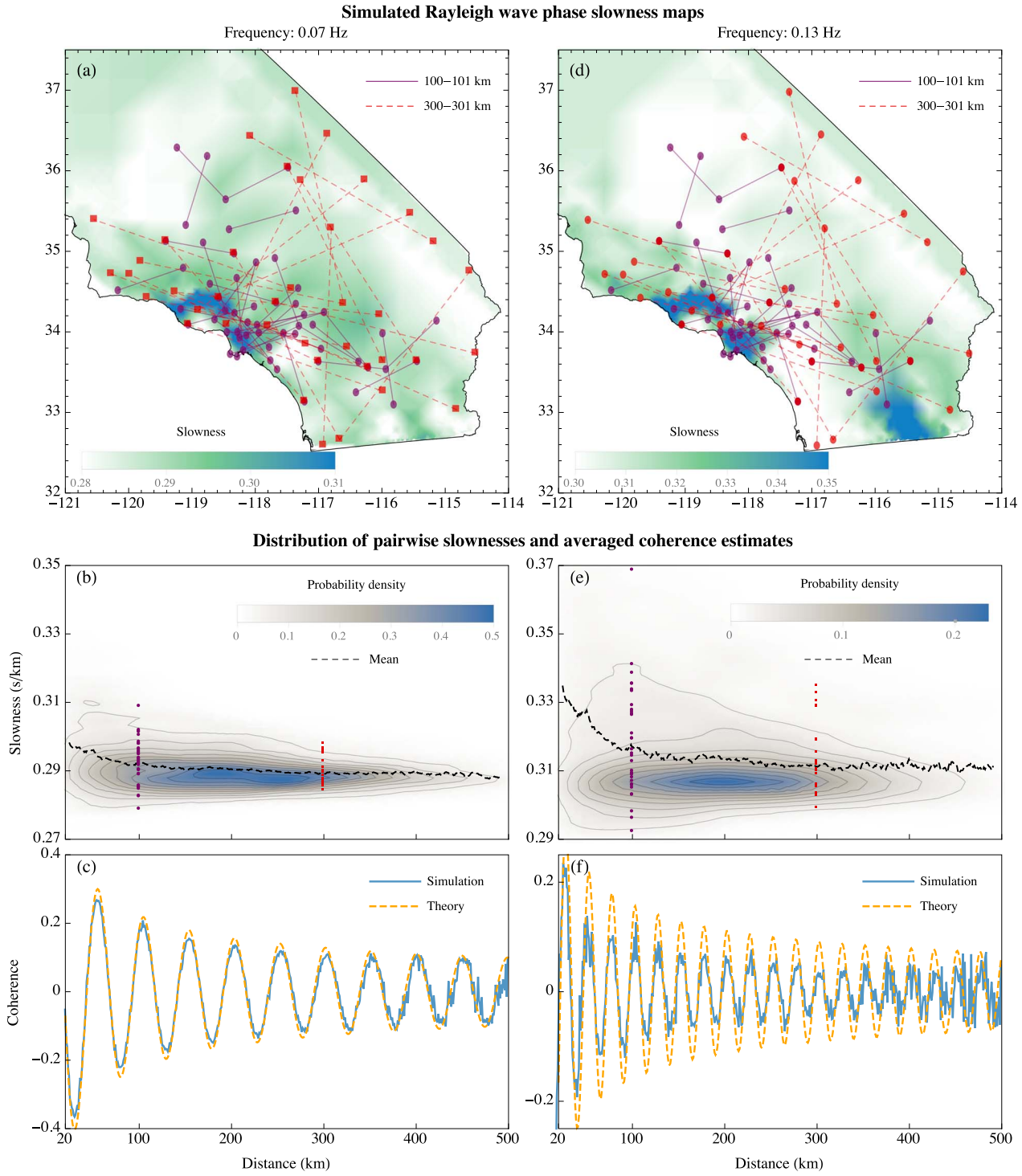

Figure 10. (a) Simulated Rayleigh wave phase slowness at 0.07 Hz for the Southern California region obtained from a dispersion analysis using a 3-D velocity model. The purple (solid) paths indicate the station pairs in the 100–101 km distance bin (D_{100} in (6)) and the red (dashed) paths for the 300–301 km bin. (b) The smoothed distribution shows the variation in effective slownesses measured by the different station pairs at a given distance, and their mean is the dashed curve. The purple and red markers highlight the slownesses corresponding to the respective paths in Figure 10a. (c) The ASC (solid) estimated as in (13) and the best fit zeroth-order Bessel model (dashed). (d–f) Same as in Figures 10a–10c but at 0.13 Hz.

signals under 0.1 s/km slowness in Figure 4b), and these are likely due to *P* waves generated when distant storms make landfall. In comparison, the contributions are more spread out at the higher frequencies. At the lower end of the band, the SCF still is predominantly due to Rayleigh waves, but the contribution from $\mathcal{R}_1$ and body waves increases with frequency.

During the Northern Hemisphere winter (December–February), contribution from body waves is higher in the upper end of the microseism band compared to the summer months (June–August). In contrast, contribution from body waves is higher at lower frequencies during the summer, likely due to the storms in the Southern Ocean which make landfall.

7. Effect of 3-D Slowness Inhomogeneities

In the previous sections, we analyzed some of the factors affecting the coherence in a laterally homogeneous medium. Here we study the effect of slowness inhomogeneities in the medium on the coherence using simulations. Specifically, we shall see that the "forced homogenization" from azimuthal averaging of station pairs at each distance distorts the coherence.

Figure 10a shows the simulated Rayleigh wave phase slowness map at 0.07 Hz for Southern California (and for 0.13 Hz in Figure 10d), obtained from a dispersion analysis [*Hermann*, 2010] using a 3-D model [*Kohler et al.*, 2003] for the density and compressional and shear velocities. From the overlaid station pairs at different distance bins (100–101 km in blue and 300–301 km in red), we see that they map out different regions at different bins. For instance, most station pairs that are 100–101 km apart fall primarily in the slower Los Angeles and Ventura sedimentary basins, whereas the pairs that are 300–301 km apart pass primarily through the faster regions. Due to the layout of the SCSN array, waves traveling between station pairs at larger distances of separation travel predominantly through high-velocity regions, spending only a small fraction of their path through the slower basin.

To understand the diversity in the slownesses sampled by different station pairs, we compute the *effective* phase slowness for each station pair (average slowness along a straight line propagation path) using the slowness map in Figures 10a and 10d. From the distribution of effective slownesses in Figures 10b and 10e, the spread in effective slownesses tends to decrease with increasing distance, which is consistent with the earlier observation that the layout of the SCSN preferentially samples the Los Angeles basin at lower separation distances. The spread also increases with frequency, and at a given distance bin, the relative standard deviation of the effective slownesses for each station pair is about 2% in Figure 10b and varies between about 10% at 20 km and about 2% at 500 km in Figure 10e.

Although this analysis sheds light on the variations in slownesses sampled by the array, the actual measured quantity is the corresponding spatial coherence which is oscillatory in nature. Due to interference from different wave numbers corresponding to the above slownesses, the ASC formed by averaging the coherences at each distance bin as in (6) or (13) will be distorted. This is evident in Figure 10f, where the ASC $\tilde{\Gamma}^{(\mathrm{sim})}$ obtained from the simulated coherences using (13) shows an apparent attenuation that is not present in the theoretical best fit SCF $\Gamma_{2\text{-D}}(2\pi f\bar{s}d)$, where $\bar{s}$ is obtained as

$$\bar{s} = \underset{s}{\operatorname{argmin}} \sum_{n} \left| \tilde{\Gamma}_{n}^{(\mathrm{sim})} - \Gamma_{2\text{-D}}(2\pi f s d_n) \right| \tag{18}$$

where the summation is over all the distance bins. The simulated ASC is also noisy, similar to that in the ASC from data (Figure 8).

It is important to note that these artifacts arise merely due to the inhomogeneity of the medium, even without considering other factors such as intrinsic attenuation, scattering, and noise field directionality. While the observations and results here are specific to Southern California and the SCSN array, the conclusions derived should be applicable to other regions with 3-D inhomogeneity at the scales being studied.

8. The Curse of Apparent Attenuation in an Inhomogeneous Medium

Although the actual expression for the apparent attenuation is likely to be complicated and intractable, we approximate it with $g(\alpha, r) = e^{-\alpha r}$ so that comparisons can be made between estimates of attenuation in other works and the apparent attenuation observed here. At each frequency, α is obtained from the

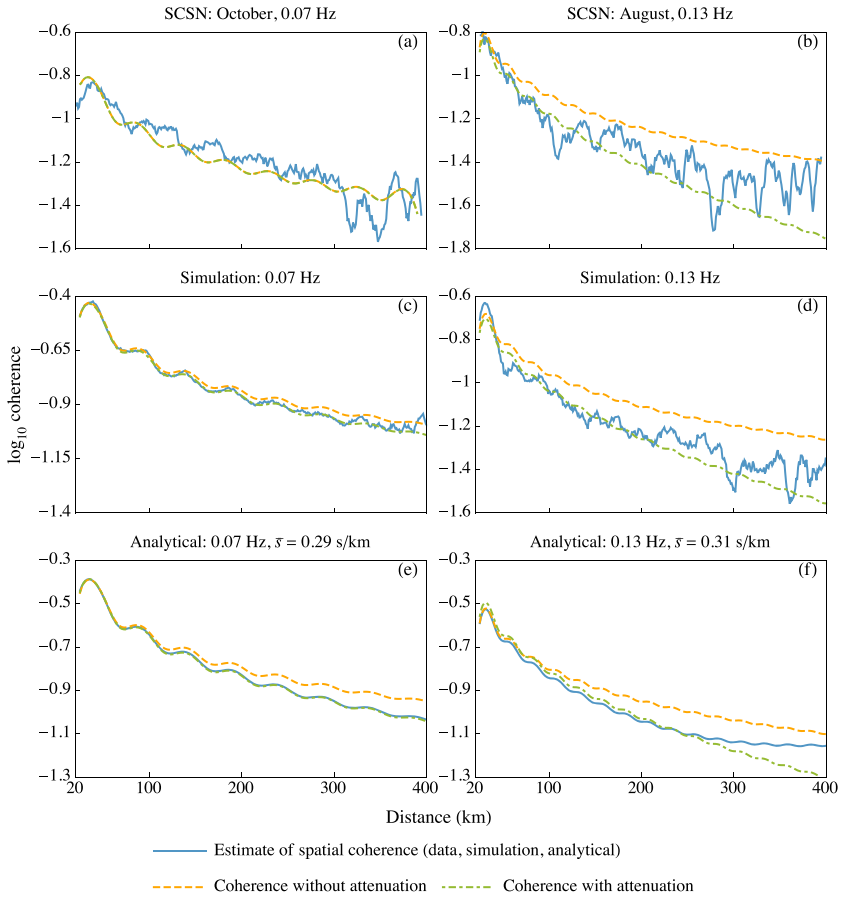

Figure 11. Log of the envelope of the ASC (solid) at 0.07 Hz and 0.13 Hz from (a and b) SCSN data, (c and d) simulations in section 7, and (e and f) analytical approximations in (21). The value of $\sigma_s/\bar{s}$ is assumed to decrease linearly from 2% at 20 km to 1% at 400 km. The best fit SCF (only $\mathcal{R}_0$) is also shown in each case with (dashed) and without attenuation (dash dotted), following *Prieto et al.* [2009].

following minimization:

$$\underset{\alpha,q}{\operatorname{argmin}} \sum_n \left| \tilde{\Gamma}_n^{(\cdot)} - q e^{-\alpha d_n} \Gamma_{2\text{-D}}(2\pi f \bar{s} d_n) \right| \tag{19}$$

where q is a scale factor that serves primarily to provide an additional degree of freedom so that the fit captures the decay and is not overly influenced by fluctuations at small separations. Figures 11a and 11b show the log of the envelope of the ASC and the best fit coherence with and without attenuation for two frequencies. These are similar to *Prieto et al.* [2009, Figure 6]. The envelopes of the ASC in Figures 11c and 11d from the simulation in section 7 bear qualitative resemblances to those from the SCSN in Figures 11a and 11b. Notably in Figures 11b and 11d, the ASC decays initially but seemingly reverses trend after about 300 km [see also *Prieto et al.*, 2009, Figure 6d]. Although this was previously interpreted as not being significant (i.e., it is just random noise), this effect is directly related to the diversity of slownesses seen in Figures 10b and 10e. In general, due to decreasing spread in the effective slowness (section 7), the coherence at greater distances has lesser attenuation due to interference but is also noisier due to decreasing number of station pairs in each bin (section 4.1). Nevertheless, the similarity of the ASCs and the respective fits in data and simulation raises the question as to whether the estimates of the attenuation coefficient obtained from data are in fact measuring the apparent attenuation due to inhomogeneities in the Earth.

While the availability of detailed 3-D velocity models for Southern California made the analysis in this section and the preceding one possible, it might not be feasible to do so for other regions where such models are not readily available. However, the insights obtained from the analysis are applicable for any suitably

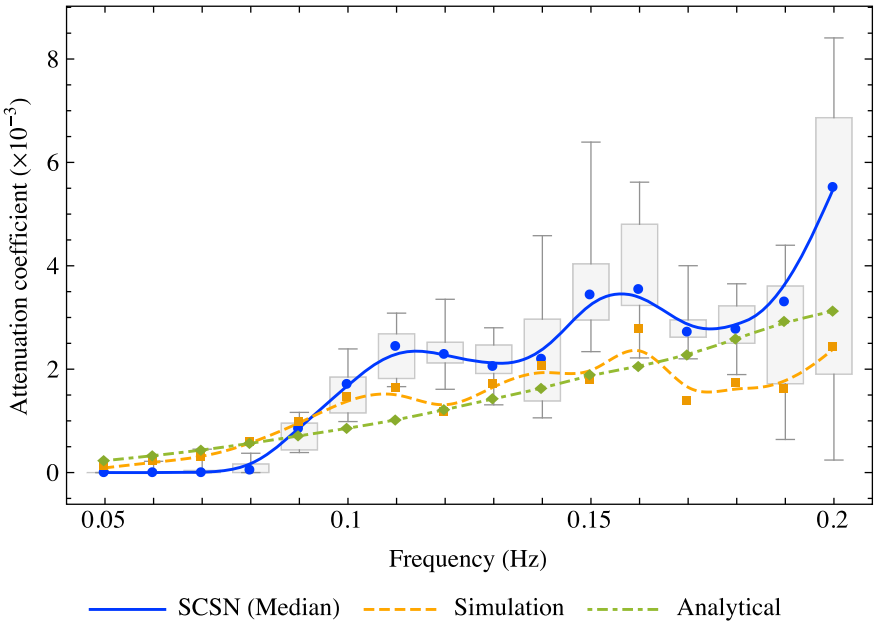

Figure 12. Comparison of apparent attenuation measured from coherence using SCSN data (solid, median), simulations with slowness inhomogeneity (dashed, section 7), and approximate analytical expressions (dash dotted, equation (21)). The lines are cubic spline fits to the points. The gray boxes are the interquartile ranges for the estimates of the attenuation coefficient from SCSN data.

inhomogeneous medium, and we demonstrate this with a simplified analytical model for an ASC resulting from an average of individual coherencies (with different slownesses). Consider an arbitrary inhomogeneous medium and array configuration such that the distribution of pairwise slownesses as in Figures 10b and 10e is uniformly distributed between $s_{\pm} = \bar{s} \pm \sqrt{3}\sigma_s$ at all frequencies, where $\bar{s}$ is the frequency-dependent mean slowness and σ_s is the standard deviation. Then using the asymptotic expansion of the zeroth-order Bessel, the expected value of the ASC at a given distance bin is

$$\begin{aligned}\mathbb{E}[\tilde{\Gamma}_n] &= \int_{-\infty}^{\infty} J_0(2\pi f d_n s)\rho(s)\,\mathrm{d}s \\ &\approx \frac{1}{2\pi\sqrt{3}\sigma_s}\int_{s_-}^{s_+}\sqrt{\frac{1}{f d_n s}}\cos\left(2\pi f d_n s - \pi/4\right)\,\mathrm{d}s \end{aligned} \tag{20}$$

where $\rho(s)$ is the probability density of s. Equation (20) can be solved in terms of the Fresnel integrals $C(z) = \int_0^z \cos(\pi t^2/2)\mathrm{d}t$ and $S(z) = \int_0^z \sin(\pi t^2/2)\mathrm{d}t$ [*Abramowitz and Stegun*, 1972, §7.3], giving

$$\mathbb{E}[\tilde{\Gamma}_n] \approx -\left[\frac{C(2\sqrt{d_n f s}) + S(2\sqrt{d_n f s})}{\sqrt{6}\pi d_n f \sigma_s}\right]_{s=s_-}^{s=s_+} \tag{21}$$

Equation (21) allows us to also vary the spread in slownesses with distance as in Figures 10b and 10e using a range-dependent σ_s. Although a uniform slowness distribution was chosen for simplicity, it is sufficient to obtain useful analytical insights on the influence of slowness inhomogeneity, and the conclusions remain the same even if a more representative distribution were used.

The apparent attenuation between (21) and (4) is a complicated relationship given by the ratio of the two expressions at a given f, d_n, and $\bar{s}$ and varies with both distance and frequency. Taking $\bar{s}$ from (18) and varying $\sigma_s/\bar{s}$ linearly from 0.02 at 20 km to 0.01 at 400 km, we repeat the minimization in (19) and the corresponding curves shown in Figures 11e and 11f. The decreasing spread in slownesses introduces an increase in the coherence (negative attenuation) after 300 km in Figures 11f, similar to Figures 11d and 11b, thus supporting the proposition that the increase seen is indeed significant and not random.

Figure 12 shows the resulting values of the attenuation coefficient obtained from the minimization in (19), for the SCSN data, simulation in section 7, and the analytical approximation in (21). All three cases result

in values of α that are physically sensible, yet in two of the cases, no intrinsic attenuation was assumed. In addition, the values are similar to each other and are of the same order of magnitude as compiled results [*Mitchell*, 1995].

It is unclear if the intrinsic medium attenuation can be untangled from these apparent attenuations. In data, additional effects such as scattering, focusing, and defocusing also will likely play a role in distorting the coherence. Given that such behavior generally is unavoidable in an unknown 3-D inhomogeneous medium, it is quite likely that the attenuation coefficients previously estimated from data are, in fact, measuring this apparent attenuation and not the intrinsic attenuation of the medium. However, as the discussion here has shown, it is useful to thoroughly analyze the interplay between the processing technique chosen, the array used, and the environment of study so that apparent attenuation effects can be identified and taken into consideration.

9. Conclusions

In this article we have performed a detailed analysis of the various factors that play a role in the estimation of spatial coherence and attenuation from seismic arrays. Primarily, we show that employing averaging at different steps in the processing is not always beneficial. For example, frequency averaging can introduce attenuation-like effects and that the effectiveness of azimuthal averaging depends on the geometry of the array.

Assuming a laterally homogeneous medium with variations only in depth, we also analyzed in detail the nature of the seismic noise observed in Southern California using the Southern California Seismic Network (SCSN). The ambient noise field shows a clear and persistent presence of fundamental and first-mode surface Rayleigh waves and body waves in the microseism band (0.05–0.2 Hz) and the resulting dispersion curves agree well with simulations. This suggests that the underlying SCF might be better modeled as a linear combination of the above wave types (with the ratios estimated from data), and we show that it indeed describes the observed coherence better than a simple zeroth-order Bessel function model which corresponds only to the fundamental mode. The interactions between the wave types in the SCF leads to beating and phase cancelation effects which could be interpreted as being due to attenuation.

Using a 3-D velocity model for Southern California, we studied the effect of slowness inhomogeneity on the estimation of spatial coherence. Due to inhomogeneity, there is diversity in the slownesses sampled by different station pairs and as a result, taking the average of the individual coherences introduces apparent attenuation (again, from interference).

Acknowledgments

This work was supported by the Office of Naval Research grants N00014-11-1-0321 and N00014-11-1-0320 and National Science Foundation grant OCE-1030022. The seismic data used in this research were recorded on the Southern California Seismic Network operated by Caltech and USGS and can be obtained from the Southern California Earthquake Data Center (SCEDC) at http://www.data.scec.org. Wave height data used in Figure 7 were obtained from NOAA's National Data Buoy Center and can be accessed at http://www.ndbc.noaa.gov/data/.

References

Abramowitz, M., and I. A. Stegun (1972), *Handbook of Mathematical Functions with Formulas, Graphs, and Mathematical Tables*, National Bureau of Standards, New York.

Aki, K. (1957), Space and time spectra of stationary stochastic waves, with special reference to microtremors, *Bull. Earthquake Res. Inst. Univ. Tokyo*, *35*, 415–457.

Asten, M. W. (2006), On bias and noise in passive seismic data from finite circular array data processed using SPAC methods, *Geophysics*, *71*(6), V153–V162.

Bensen, G. D., M. H. Ritzwoller, M. P. Barmin, A. L. Levshin, F. Lin, M. P. Moschetti, N. M. Shapiro, and Y. Yang (2007), Processing seismic ambient noise data to obtain reliable broad-band surface wave dispersion measurements, *Geophys. J. Int.*, *169*, 1239–1260.

Brooks, L. A., J. Townend, P. Gerstoft, S. Bannister, and L. Carter (2009), Fundamental and higher-mode Rayleigh wave characteristics of ambient seismic noise in New Zealand, *Geophys. Res. Lett.*, *36*, L23303, doi:10.1029/2009GL040434.

Capon, J. (1969), High-resolution frequency-wavenumber spectrum analysis, *Proc. IEEE*, *57*(8), 1408–1418.

Cox, H. (1973), Spatial correlation in arbitrary noise fields with application to ambient sea noise, *J. Acoust. Soc. Am.*, *54*(5), 1289–1301.

Cupillard, P., and Y. Capdeville (2010), On the amplitude of surface waves obtained by noise correlation and the capability to recover the attenuation: A numerical approach, *Geophys. J. Int.*, *181*, 1687–1700.

Denolle, M., E. Dunham, G. Prieto, and G. Beroza (2013), Ground motion prediction of realistic earthquake sources using the ambient seismic field, *J. Geophys. Res. Solid Earth*, *118*, 2102–2118, doi:10.1029/2012JB009603.

Denolle, M., E. Dunham, G. Prieto, and G. Beroza (2014), Strong ground motion prediction using virtual earthquakes, *Science*, *343*(6169), 399–403.

Eckart, C. H. (1953), The theory of noise in continuous media, *J. Acoust. Soc. Am.*, *25*(2), 195–199.

Ekström, G., G. A. Abers, and S. C. Webb (2009), Determination of surface-wave phase velocities across USarray from noise and Aki's spectral formulation, *Geophys. Res. Lett.*, *36*, L18301, doi:10.1029/2009GL039131.

Fry, B., F. Deschamps, E. Kissling, L. Stehly, and D. Giardini (2010), Layered azimuthal anisotropy of Rayleigh wave phase velocities in the European Alpine lithosphere inferred from ambient noise, *Earth Planet. Sci. Lett.*, *297*(1), 95–102.

Gallego, A., M. Panning, R. Russo, D. Comte, V. Mocanu, R. Murdie, and J. Vandecar (2011), Azimuthal anisotropy in the Chile Ridge subduction region retrieved from ambient noise, *Lithosphere*, *3*(6), 393–400.

Gerstoft, P., and T. Tanimoto (2007), A year of microseisms in Southern California, *Geophys. Res. Lett.*, *34*, L20304, doi:10.1029/2007GL031091.

Gerstoft, P., K. G. Sabra, P. Roux, W. A. Kuperman, and M. C. Fehler (2006a), Green's functions extraction and surface-wave tomography from microseisms in Southern California, *Geophysics*, *71*, SI23–SI31.
Gerstoft, P., M. C. Fehler, and K. G. Sabra (2006b), When Katrina hit California, *Geophys. Res. Lett.*, *33*, L17308, doi:10.1029/2006GL027270.
Gerstoft, P., P. M. Shearer, N. Harmon, and J. Zhang (2008), Global P, PP, and PKP wave microseisms observed from distant storms, *Geophys. Res. Lett.*, *35*, L23306, doi:10.1029/2008GL036111.
Gualtieri, L., E. Stutzmann, V. Farra, Y. Capdeville, M. Schimmel, F. Ardhuin, and A. Morelli (2014), Modelling the ocean site effect on seismic noise body waves, *Geophys. J. Int.*, doi:10.1093/gji/ggu042.
Harmon, N., D. Forsyth, and S. Webb (2007), Using ambient seismic noise to determine short-period phase velocities and shallow shear velocities in young oceanic lithosphere, *Bull. Seismol. Soc. Am.*, *97*(6), 2009–2023.
Harmon, N., P. Gerstoft, C. A. Rychert, and G. A. Abers (2008), Phase velocities from seismic noise using beamforming and cross correlation in Costa Rica and Nicaragua, *Geophys. Res. Lett.*, *35*, L19303, doi:10.1029/2008GL035387.
Harmon, N., C. Rychert, and P. Gerstoft (2010), Distribution of noise sources for seismic interferometry, *Geophys. J. Int.*, *183*, 1470–1484.
Haubrich, R. A., and K. McCamy (1969), Microseisms: Coastal and pelagic sources, *Rev. Geophys.*, *7*(3), 539–571.
Hermann, R. B. (2010), Computer programs in seismology, version 3.30. *Saint Louis University*.
Huber, P. J. (1981), *Robust Statistics*, 380 pp., John Wiley & Sons, New York.
Kennett, B., E. Engdahl, and R. Buland (1995), Constraints on seismic velocities in the Earth from traveltimes, *Geophys. J. Int.*, *122*(1), 108–124.
Kohler, M., H. Magistrale, and R. Clayton (2003), Mantle heterogeneities and the SCEC three-dimensional seismic velocity model version 3, *Bull. Seismol. Soc. Am.*, *93*, 757–774.
Larose, E., A. Derode, M. Campillo, and M. Fink (2004), Imaging from one-bit correlations of wideband diffuse wave fields, *J. Appl. Phys.*, *95*, 8393–8399.
Lawrence, J. F., and G. A. Prieto (2011), Attenuation tomography of the western United States from ambient noise, *J. Geophys. Res.*, *116*, B06302, doi:10.1029/2010JB007836.
Lawrence, J. F., M. Denolle, K. J. Seats, and G. A. Prieto (2013), A numeric evaluation of attenuation from ambient noise correlation functions, *J. Geophys. Res. Solid Earth*, *118*, 6134–6145, doi:10.1002/2012JB009513.
Lin, F.-C., M. P. Moschetti, and M. H. Ritzwoller (2008), Surface wave tomography of the western United States from ambient seismic noise: Rayleigh and Love wave phase velocity maps, *Geophys. J. Int.*, *173*(1), 281–298, doi:10.1111/j.1365-246X.2008.03720.x.
Lin, F.-C., V. C. Tsai, and M. H. Ritzwoller (2012), The local amplification of surface waves: A new observable to constrain elastic velocities, density, and anelastic attenuation, *J. Geophys. Res.*, *117*, B06302, doi:10.1029/2012JB009208.
Liu, X., and Y. Ben-Zion (2013), Theoretical and numerical results on effects of attenuation on correlation functions of ambient seismic noise, *Geophys. J. Int.*, *194*(3), 1966–1983.
Lobkis, O. I., and R. L. Weaver (2001), On the emergence of the Green's function in the correlations of a diffuse field, *J. Acoust. Soc. Am.*, *110*, 3011–3017.
Matzel, E. M. (2008), Attenuation tomography using ambient noise correlation, *Seismol. Res. Lett.*, *79*, 358.
Mitchell, B. J. (1995), Anelastic structure and evolution of the continental crust and upper mantle from seismic surface wave attenuation, *Rev. Geophys.*, *33*(4), 441–462.
Nakahara, H. (2012), Formulation of the spatial autocorrelation (SPAC) method in dissipative media, *Geophys. J. Int.*, *190*, 1777–1783.
Nishida, K., H. Kawakatsu, Y. Fukao, and K. Obara (2008), Background Love and Rayleigh waves simultaneously generated at the Pacific Ocean floors, *Geophys. Res. Lett.*, *35*, L16307, doi:10.1029/2008GL034753.
Prieto, G. A., and G. C. Beroza (2008), Earthquake ground motion prediction using the ambient seismic field, *Geophys. Res. Lett.*, *35*, L14304, doi:10.1029/2008GL034428.
Prieto, G. A., J. F. Lawrence, and G. C. Beroza (2009), Anelastic Earth structure from the coherency of the ambient seismic noise field, *J. Geophys. Res.*, *114*, B07303, doi:10.1029/2008JB006067.
Riahi, N., and E. H. Saenger (2014), Rayleigh and Love wave anisotropy in Southern California using seismic noise, *Geophys. Res. Lett.*, *41*, 363–369, doi:10.1002/2013GL058518.
Roux, P., K. G. Sabra, W. Kuperman, and A. Roux (2005a), Ambient noise cross correlation in free space: Theoretical approach, *J. Acoust. Soc. Am.*, *117*, 79–84.
Roux, P., K. G. Sabra, P. Gerstoft, W. Kuperman, and M. C. Fehler (2005b), P-waves from cross-correlation of seismic noise, *Geophys. Res. Lett.*, *32*, L19303, doi:10.1029/2005GL023803.
Sabra, K. G., P. Gerstoft, P. Roux, W. Kuperman, and M. C. Fehler (2005), Surface wave tomography from microseisms in Southern California, *Geophys. Res. Lett.*, *32*, L14311, doi:10.1029/2005GL023155.
Shapiro, N. M., M. Campillo, L. Stehly, and M. H. Ritzwoller (2005), High-resolution surface-wave tomography from ambient seismic noise, *Science*, *307*, 1615–1618.
Snieder, R., and E. Larose (2013), Extracting Earth's elastic wave response from noise measurements, *Annu. Rev. Earth Planet. Sci.*, *41*(1), 183–206.
Tsai, V. C. (2009), On establishing the accuracy of noise tomography travel-time measurements in a realistic medium, *Geophys. J. Int.*, *178*, 1555–1564.
Tsai, V. C. (2011), Understanding the amplitudes of noise correlation measurements, *J. Geophys. Res.*, *116*, B09311, doi:10.1029/2011JB008483.
van Trees, H. L. (2002), *Detection, Estimation, and Modulation Theory Part IV: Optimum Array Processing*, John Wiley & Sons, New York.
Walker, S. C. (2012), A model for spatial coherence from directive ambient noise in attenuating, dispersive media, *J. Acoust. Soc. Am.*, *132*(1), EL15–EL21.
Walker, S. C., and M. J. Buckingham (2012), Spatial coherence and cross correlation of three-dimensional ambient noise fields in the ocean, *J. Acoust. Soc. Am.*, *131*(2), 1079–1086.
Wapenaar, K., D. Draganov, R. Snieder, X. Campman, and A. Verdel (2010a), Tutorial on seismic interferometry: Part 1—Basic principles and applications, *Geophysics*, *75*(5), 75A195–75A209.
Wapenaar, K., E. Slob, R. Snieder, and A. Curtis (2010b), Tutorial on seismic interferometry: Part 2—Underlying theory and new advances, *Geophysics*, *75*(5), 75A211–75A227.
Weaver, R. L. (2011), On the amplitudes of correlations and the inference of attenuations, specific intensities and site factors from ambient noise, *C.R. Geosci.*, *343*, 615–622.
Weaver, R. L., and O. I. Lobkis (2001), Ultrasonics without a source: Thermal fluctuation correlations at MHz frequencies, *Phys. Rev. Lett.*, *87*, 134301.

Weemstra, C., L. Boschi, A. Goertz, and B. Artman (2013), Seismic attenuation from recordings of ambient noise, *Geophysics*, *78*(1), Q1–Q14.

Yao, H., and R. D. Van Der Hilst (2009), Analysis of ambient noise energy distribution and phase velocity bias in ambient noise tomography, with application to SE Tibet, *Geophys. J. Int.*, *179*(2), 1113–1132.

Yao, H., R. D. van Der Hilst, and M. V. De Hoop (2006), Surface-wave array tomography in SE Tibet from ambient seismic noise and two-station analysis—I. Phase velocity maps, *Geophys. J. Int.*, *166*(2), 732–744.

Zhang, J., and X. Yang (2013), Extracting surface wave attenuation from seismic noise using correlation of the coda of correlation, *J. Geophys. Res. Solid Earth*, *118*, 2191–2205, doi:10.1002/jgrb.50186.

Zhang, J., P. Gerstoft, and P. D. Bromirski (2010), Pelagic and coastal sources of P-wave microseisms: Generation under tropical cyclones, *Geophys. Res. Lett.*, *37*, L15301, doi:10.1029/2010GL044288.